PCCP

ROYAL SOCIETY OF CHEMISTRY

PAPER

View Article Online
View Journal | View Issue

Cite this: *Phys. Chem. Chem. Phys.*, 2025, **27**, 24195

Bandgap engineering of $SrZrS_3$ chalcogenide perovskite *via* substitutional doping for photovoltaic applications: a first-principles DFT study

Henry I. Eya, [a] Robert Patterson [b] and Nelson Y. Dzade *[a]

Strontium zirconium sulfide ($SrZrS_3$) has garnered significant attention for photovoltaic (PV) applications due to its excellent optoelectronic properties, high chemical and moisture stability, and non-toxicity. However, the bandgaps of both the α- and β-phases lie outside the optimum ranges for both single-junction solar cells (SJSCs) and tandem solar cells (TSCs), thereby limiting their applications in PV technologies. In this study, we employed hybrid density functional theory to engineer the band gaps of α- and β-$SrZrS_3$ through substitutional doping. We considered three dopants (Hf, Sn, and Ti) at the Zr site of $SrZrS_3$ with varying doping concentrations and investigated their effects on the structural, electronic, and optical properties of the materials. We found that Sn and Ti doping effectively lowers the band gaps of both α- and β-$SrZrS_3$, whereas Hf doping increases them. For x values up to 0.25, the band gaps of the α-$SrZr_{1-x}Sn_xS_3$ and α-$SrZr_{1-x}Ti_xS_3$ are within the optimum range for SJSCs, and those of β-$SrZr_{1-x}Sn_xS_3$ and β-$SrZr_{1-x}Ti_xS_3$ lie within the optimum range for Si/perovskite as well as perovskite/perovskite TSCs. The three dopants exhibited significant effects on the optical properties of both α- and β-$SrZrS_3$, including the absorption coefficient, energy-loss functions, reflectivity, and refractivity spectra. Thermodynamic stability analysis revealed that for both phases, $SrZr_{1-x}Hf_xS_3$ can be synthesized *via* exothermic processes, whereas the formation of $SrZr_{1-x}Ti_xS_3$ and $SrZr_{1-x}Sn_xS_3$ is endothermic and hence, not thermodynamically favorable. Further analysis showed that $SrZr_{1-x}Ti_xS_3$ in both α- and β-phases are stable under thermodynamic equilibrium conditions, whereas $SrZr_{1-x}Sn_xS_3$ is prone to dissociation into ternary phases ($SrZrS_3$ and $SrSnS_3$), especially at higher doping concentrations. These results show that Ti doping is effective in tuning the band gaps of α- and β-$SrZrS_3$ toward the optimal values for PV applications.

Received 24th July 2025,
Accepted 21st October 2025

DOI: 10.1039/d5cp02689j

rsc.li/pccp

1. Introduction

Perovskite solar cells (PSCs) have emerged as one of the most promising photovoltaic technologies to compete with the dominant Si-based solar cells. Since the first perovskite solar cell was reported in 2009, the efficiency has witnessed an unprecedented increase from 3.8% to a verified 26.1% at one Sun.[1,2] This high photovoltaic (PV) performance has been attributed to the excellent electronic and optical properties of the perovskite materials, including high mobility carriers, high light absorption coefficient, long carrier diffusion length, low trap density, and tunable band gaps.[3–5] In addition to their high efficiency, PSCs have been recognized as a low-cost technology because they can be fabricated *via* various low-cost methods, such as ambient spray coating, chemical vapor deposition (CVD), radio-frequency magnetron sputtering, electrodeposition, chemical bath deposition, and thermal evaporation.[6–10] Because of their relatively large and tunable band gaps, perovskites have also been recently identified as promising partner materials for Si-based tandem solar cells. Perovskite/Si tandem solar cells have attracted significant attention owing to their potential to achieve very high efficiency (up to 46%), surpassing the Shockley–Queisser efficiency limit for single-junction solar cells (SJSCs).[11–13] Recent studies have reported a verified efficiency of 33.9% for a four-terminal Si/perovskite TSC.[13,14] Perovskite/perovskite TSCs with efficiency exceeding that of SJSCs have also been reported.[15,16] However, the commercialization of perovskite-based solar cells has been hindered by the instability and toxicity associated with organic–inorganic halide perovskites (OIHPs). Therefore, ongoing efforts are directed either at

[a] *The Department of Energy and Mineral Engineering, The Pennsylvania State University, USA. E-mail: nxd5313@psu.edu*
[b] *School of Photovoltaic and Renewable Energy Engineering, University of New South Wales, Australia*

improving the stability of OIHPs or discovering alternative perovskite materials with improved stability.

Recently, chalcogenides perovskites (CPs) with the general formula ABX_3 (where A is a group II cation (Ba^{2+}, Ca^{2+}, or Sr^{2+}), B a group IV cation (Zr^{4+}, Ti^{4+}, or Hf^{4+}), and X a chalcogen anion (S^{2-} or Se^{2-})) have emerged as attractive alternatives to OIHPs owing to their high chemical and thermal stability, nontoxicity, earth-abundant composition, and excellent optoelectronic properties.[17–20] Several CPs have been predicted through theoretical studies for thin-film solar cells. For instance, Sun *et al.* predicted $CaTiS_3$, $BaZrS_3$, $CaZrSe_3$, and $CaHfSe_3$ with distorted perovskite structures and showed that they possess ideal band gaps and high optical absorption for solar cell applications.[21] Basera *et al.* simulated sulfide chalcogenide perovskites ABS_3 (A = Ba, Ca, and Sr; B = Hf and Sn) using density functional theory (DFT) methods and reported that they possess exciton binding energies larger than those of three-dimensional (3D) inorganic–organic hybrid perovskites.[22] CPs have also been successfully synthesized using various techniques. Niu *et al.* synthesized α-$SrZrS_3$, β-$SrZrS_3$, $BaZrS_3$, Ba_2ZrS_4, and $Ba_3Zr_2S_7$ with several structural types, including distorted perovskite, needle-like, and Ruddlesden–Popper phases, and reported that they exhibit high thermal stability at temperatures up to 550 °C.[18]

$SrZrS_3$ has great potential for optoelectronic and photovoltaic applications. According to previous studies, this material exists in two crystal phases: α-$SrZrS_3$ and β-$SrZrS_3$, both of which are stable under ambient conditions.[18–21] These two phases differ significantly in terms of structural and optoelectronic properties. The NH_4CdCl_3-type phase (*i.e.*, α-$SrZrS_3$) exhibits a needle-like crystal structure, whereas the $GdFeO_3$-type phase (*i.e.*, β-$SrZrS_3$) possesses a distorted perovskite structure. In addition, α-$SrZrS_3$ has a bandgap of approximately 1.53 eV, which is close to the optimum bandgap for SJSCs (~1.1–1.4 eV),[23,24] whereas that of β-$SrZrS_3$ ranges from 1.98 to 2.13 eV, which is much higher than the ideal value for optimum solar absorption.[18,19,25,26] However, according to Sun *et al.*, materials with distorted perovskite structures generally exhibit better optical absorption properties than those with needle-like structures,[21] indicating that both α- and β-$SrZrS_3$ are promising for PV applications. In addition, the large bandgap of β-$SrZrS_3$ is attractive for use in tandem solar cells. However, the value exceeds the optimal range for maximum efficiency in both Si/perovskite and perovskite/perovskite TSCs.[11,13,15,16] Therefore, to ensure optimal PV performance for both α- and β-$SrZrS_3$, it is necessary to tune their band gaps to the optimum values required for PV applications.

The optoelectronic properties of various semiconductors, including perovskites, have been successfully tuned by adding impurity atoms into their crystal structures, a technique known as doping. According to He *et al.*, owing to the tunable crystal structure of perovskites (ABX_3), the bandgap can be precisely controlled *via* doping at the A, B, and/or X sites, resulting in high fluorescence quantum yields and emission in the visible and near-infrared regions.[27] Specifically, B-site doping can significantly affect the bandgap and the channel for radiative recombination in perovskites. Meng *et al.* achieved a 16.48% decrease in the bandgap of $BaZrS_3$ (from 1.76 to 1.47 eV) by replacing ~10% of Zr with Ti.[28] Yu *et al.* also reported Fe- and Mn-doped $BaZrS_3$ ($BaZr_{1-x}Mn_xS_3$ and $BaZr_{1-x}Mn_xS_3$) with band gaps of 1.58 and 1.63 eV for a doping concentration of approximately 5%.[29] Wei *et al.* synthesized Ti-doped $BaZrS_3$ ($BaZr_{1-x}Ti_xS_3$) and reported a decrease in bandgap from 1.78 to 1.51 eV for a doping atom percentage of 4%.[30] The bandgap of β-$SrZrS_3$ has also been tuned by doping antimony (Sb) into the Zr site; however, the authors recorded an increase in the bandgap.[31] The band gaps and other optoelectronic properties of several other perovskite materials have also been successfully tuned through doping.[32–35]

In this study, we employed first-principles density functional theory (DFT) calculations to investigate the effects of various dopant cations, including Hf, Ti, and Sn, on the band gaps and optical properties of both $SrZrS_3$ phases. We varied the doping concentration (from 0 to 50 atom%) to verify its effects on the material properties. We also investigated the thermodynamic stability of the pristine material by determining the range of chemical potentials in which the material is stable. Furthermore, we studied the formability and stability of the doped materials by calculating their defect formation and dissociation energies, respectively. Our predicted reduction in band gaps and enhanced optical properties indicate that Sn- and Ti-doped $SrZrS_3$ are promising materials for photovoltaic applications.

Nelson Y. Dzade

Nelson Dzade is an assistant professor, DOE early career researcher, and the chair of the undergraduate energy engineering program in the John and Willie Leone Family Department of Energy and Mineral Engineering at Penn State. He leads the Materials and Minerals Theory Group, which specializes in the development and application of advanced theoretical methods to unravel structure–property-performance relationships in solid-state materials and minerals for applications in solar cells, catalysis, batteries, and critical minerals beneficiation. He was an EPSRC innovation research fellow at Cardiff University and a postdoctoral scholar at Utrecht University. He holds a PhD in Computational Materials Science from University College London, UK.

2. Computational details

We performed first-principles calculations based on DFT as implemented in the Vienna *ab initio* simulation package (VASP), a plane-wave-based code.[36,37] The projector augmented wave (PAW) pseudopotentials were employed to describe the

interactions between the ion cores and valence electrons.[38,39] First, we obtained the crystallography information files (CIFs) of the two phases of $SrZrS_3$ from the Materials Project database[20,40] and optimized them using the generalized gradient approximation (GGA) Perdew–Burke–Ernzerhof (PBE) functional.[41] Monkhorst–Pack k-point meshes of $5 \times 7 \times 3$ and $5 \times 5 \times 3$ were employed for the α- and β-phases, respectively. The total energies of the systems and the residual ionic forces were converged within 10^{-6} eV and 10^{-3} eV Å^{-1}, respectively, using a plane-wave cutoff energy of 600 eV. Because the PBE functional is known to underestimate the band gaps of semiconductors, the density of state (DOS), band structure, and optical property calculations were performed using the Hartree–Fock screened hybrid functional (HSE06). Hartree–Fock exchange fractions of 32% and 25% were employed for the α- and β-phases, respectively, as they predict the bandgap of the studied materials in close agreement with the experiments. Spin–orbit coupling (SOC) has not been considered in calculations, as previous studies have shown that it has a negligible effect on the electronic structure of chalcogenide perovskites.[22,42] The projected density of states (PDOS) and band structures were plotted using SUMO software.[43]

The linear optical properties of the materials were determined from the frequency-dependent complex dielectric function $\varepsilon(w)$, which is expressed as follows:

$$\varepsilon(w) = \varepsilon_1(w) + i\varepsilon_2(w), \quad (1)$$

where $\varepsilon_1(w)$ and $\varepsilon_2(w)$ are the real and imaginary parts of the dielectric function, respectively, and w is the photon frequency. The frequency-dependent linear optical spectra, including the absorption coefficient $\alpha(w)$, refractive index $n(w)$, reflectivity $R(w)$, and energy-loss function $L(w)$, were obtained from $\varepsilon_1(w)$ and $\varepsilon_2(w)$ as follows:

$$\alpha(w) = \frac{\sqrt{2w}}{c}\left[\sqrt{\varepsilon_1{}^2 + \varepsilon_2{}^2} - \varepsilon_1\right]^{\frac{1}{2}} \quad (2)$$

$$n(w) = \left[\frac{\sqrt{\varepsilon_1{}^2 + \varepsilon_2{}^2} + \varepsilon_1}{2}\right]^{\frac{1}{2}} \quad (3)$$

$$R(w) = \frac{(n-1)^2 + k^2}{(n+1)^2 + k^2} \quad (4)$$

$$L(w) = \frac{\varepsilon_2}{\varepsilon_1{}^2 + \varepsilon_2{}^2} \quad (5)$$

where c is the speed of light in a vacuum. These optical properties were extracted using VASPKIT.[44]

To explore different doping concentrations, supercells of $1 \times 2 \times 1$ and $2 \times 1 \times 1$ were constructed for the α- and β-phases, respectively, resulting in a total of 40 atoms per cell. Geometrical optimization was performed on the supercells using the PBE function with k-point meshes of $5 \times 5 \times 3$ and $3 \times 7 \times 5$ for the α- and β-phases, respectively. Furthermore, 1, 2, 3, and 4 Zr atoms in the supercells were substituted with dopant atoms (Hf, Sn, and Ti), corresponding to doping concentrations of 12.5%, 25%, 37.5%, and 50% atom%, respectively. Considering that all Zr sites are identical in both structures, the doping sites were randomly selected. For cases where more than one Zr atoms were substituted, we tested and found that when the dopant atoms are far away from each other, the structure is 0.16 eV energetically more stable than when they are closer to each other. Therefore, we ensured that the selected sites for multiple dopants were well spread out uniformly throughout the structures (Fig. S1 and S2). The doped structures were optimized using the same settings as the pristine supercells. The electronic and optical properties were also obtained using HSE06 with the same Hartree–Fock exchange fractions as for the unit cells. Considering the computational cost of the hybrid functional, lower Monkhorst–Pack k-point meshes of $3 \times 3 \times 1$ and $1 \times 5 \times 3$ were used for the DOS, band structure, and optical property calculations.

3. Results and discussion

3.1. Structural and electronic properties of pristine $SrZrS_3$

The two $SrZrZ_3$ phases crystallize in the orthorhombic crystal system (space group: *Pnma*).[26] Fig. 1(a) and (d) show the optimized structures of the pristine α- and β-$SrZrS_3$. The α-phase forms a needle-like NH_4CdCl_3 type structure with one-dimensional double chains of edge-sharing ZrS_6 octahedra, and the Sr atoms are ninefold coordinated with S atoms. The β-phase forms the $GdFeO_3$-type distorted perovskite structure comprising three-dimensionally connected corner-sharing Zr octahedra and Sr atoms that are eightfold coordinated with S atoms. The obtained lattice parameters and crystal volumes for the two phases are consistent with both previously reported theoretical and experimental values, as listed in Table S1.[20,26] Fig. 1(b), (c), (e), and (f) also show the projected DOS and band structures of the pristine materials obtained using the HSE06 functional, and Table S1 lists their bandgaps. The α- and β-$SrZrS_3$ exhibited direct band gaps as both the valence band maximum (VBM) and conduction band minimum (CBM) are located at the Γ point in the Brillouin zone (Fig. 1(c) and (f)). The bandgap energies are predicted at 1.56 and 2.03 eV, which agree well with previous theoretical and experimental results.[19,26,45] The PDOS reveals that for both phases, the VBM and CBM are dominated by S-p and Zr-d orbitals, respectively, which are also consistent with our previous results.[26]

3.2. Structural and electronic properties of doped $SrZrS_3$

Herein, we considered three substitutional elements (Hf, Sn, and Ti) in the Zr site for both α-$SrZrS_3$ and β-$SrZrS_3$, resulting in $SrZr_{1-x}Hf_xS_3$, $SrZr_{1-x}Sn_xS_3$, $SrZr_{1-x}Ti_xS_3$ systems (x = 0.00, 0.125, 0.25, 0.375, and 0.50), where x values of 0.125, 0.25, 0.375, and 0.50 correspond to the systems in which 1, 2, 3, and 4 atoms out the 8 Zr atoms in the supercells are replaced with the dopant atoms, respectively. We studied the effects of the dopants on the structural, electronic, and optical properties of the materials, and the results are discussed next.

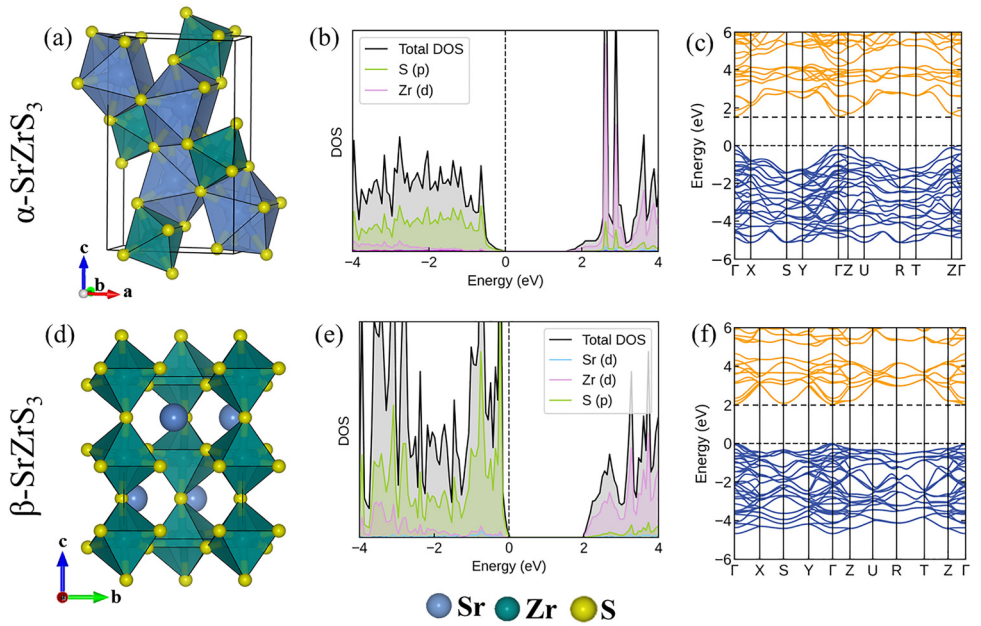

Fig. 1 (a) and (d) Optimized crystal structures, (b) and (e) projected density of states (PDOS), and (c) and (f) band structures of α-$SrZrS_3$ and β-$SrZrS_3$ perovskites.

3.2.1. Structural properties of doped $SrZrS_3$. Fig. 2(a)–(f) show the optimized supercell crystal structures of the Hf-, Sn-, and Ti-doped α- and β-$SrZrS_3$ with 12.5 atom% (Fig. S1 and S2 show those of the systems with doping concentration of 25, 37.5, and 50 atom%), and Table S1 lists the supercell lattice parameters and volumes for the pristine and doped systems. Substitutional doping of both the α- and β-$SrZrS_3$ phases with Hf and Ti resulted in a slight shrinkage of the supercells. As the doping concentration increased from 0% to 50%, the lattice parameters generally decreased, resulting in a linear decrease in the cell volumes, as shown in Fig. 2(g). The shrinkage in volume is attributed to the fact that the ionic radius of Hf^{4+} (0.71 Å) and Ti^{4+} (0.605 Å) is smaller than that of Zr^{4+} (0.72 Å).[46,47] This is consistent with previous reports on Ti-doped $BaZrS_3$, where the lattice constants were found to decrease with increasing Ti content, thereby decreasing the volume of the system.[30,48] Xu *et al.* also reported a decrease in lattice parameters for Ag-doped $CH_3NH_3PbI_3$ perovskite, which they attributed to the smaller ionic radius of Ag^+ compared to that of Pb^{2+}.[49] In contrast, although the radius of Sn^{4+} (0.69 Å) is slightly smaller than that of Zr^{4+}, we observed a slight increase in the lattice parameters of both the α- and β-$SrZr_{1-x}Sn_xS_3$ with increasing doping concentrations, resulting in an overall increase in supercell volume, as shown in Fig. 2(g).

Comparing the three dopants in α-$SrZrS_3$, the Ti-doped systems generally showed a more significant change in the supercell volume, followed by the Sn-doped systems. The percentage change in volume (ΔV, Table S1) for α-$SrZr_{1-x}Ti_xS_3$ varied from −1.04% to −4.20% as x increased from 0.125 to 0.5 (negative values indicate shrinkages), whereas that for

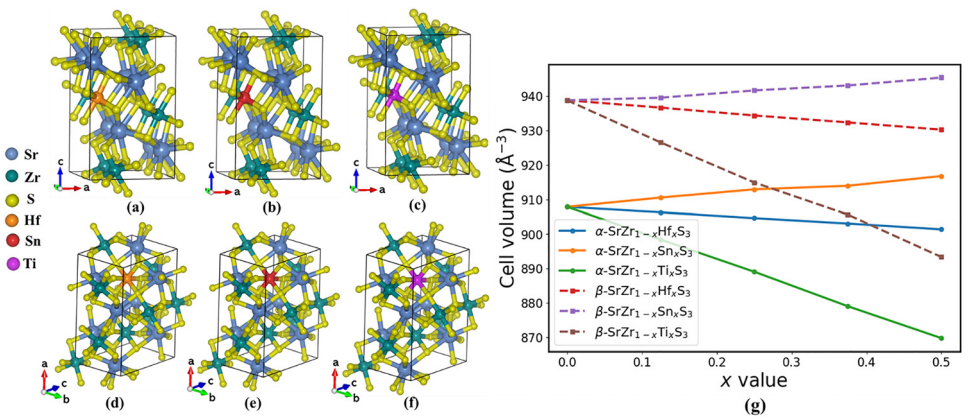

Fig. 2 Optimized structures of (a) and (d) α- and β-$SrZr_{1-x}Hf_xS_3$, (b) and (e) α- and β-$SrZr_{1-x}Sn_xS_3$, and (c) and (f) α- and β-$SrZr_{1-x}Ti_xS_3$. (g) Variation of supercell volume with doping concentration x. Supercell sizes for the α- and β-phases are 1 × 2 × 1 and 2 × 1 × 1, respectively.

α-$SrZr_{1-x}Hf_xS_3$ only varied from −0.18% to −0.71%. This order is consistent with the decreasing order of the ionic radii of dopants ($r_{Zr} > r_{Hf} > r_{Sn} > r_{Ti}$). Similarly, for the β-phase, the change in volume for the Ti-doped systems is higher than that of Sn- and Hf-doped systems. However, that of the Hf-doped systems is higher than that of the Ti-doped system. Furthermore, considering the supercell angles of the pure and doped systems, there was no significant distortion of the α-phase. In contrast, the β-$SrZrS_3$ structure was appreciably distorted by the addition of the dopants, especially at high doping concentrations.

In perovskite materials, structural stability and formability are essential considerations. Hence, when considering dopant choices, it is paramount to explore their effects on the structural stability and formability of the parent material. For an ABX_3 perovskite system, the stability and formability can be predicted purely based on geometrical considerations (*i.e.*, from the ionic radii of the constituent elements). The formability of a perovskite structure can be predicted by the Goldschmidt tolerance factor t and the octahedral factor u, which are expressed as follows:[50–52]

$$t = \frac{r_A + r_X}{\sqrt{2}(r_B + r_X)}, \quad (6)$$

$$u = \frac{r_B}{r_X}, \quad (7)$$

where r_A, r_B, and r_X are the ionic radii of the A cation, B cation, and X anion, respectively. An orthorhombic perovskite structure forms when $0.91 \leq t \leq 1$ and $u \geq 0.41$, a distorted perovskite is formed when $0.71 \leq t \leq 0.91$ and $u \geq 0.41$, and a non-perovskite structure is formed when $t > 1$, $t < 0.71$, or $u < 0.41$.[50] However, several perovskite structures have been successfully synthesized for u values less than 0.41. For example, $BaZrS_3$, which has a u value of 0.39, has been successfully synthesized in the perovskite structure.[53,54] Herein, we calculated t and u for both the pure $SrZrS_3$ system using the ionic radii of Sr^{2+} with cubic coordination (1.26 Å), octahedral Zr^{4+} (0.72 Å), and octahedral S^{2-} (1.84 Å).[46] For the doped systems, because the dopants occupy the B sites, r_B in the eqn (7) and (8) were calculated as the arithmetic mean of the Zr and dopant radii. For example, for the $SrZr_{1-x}Hf_xS_3$ system, $r_B = (1 - x)r_{Zr} + xr_{Hf}$. Here, the radii of the octahedral Hf^{4+}, Sn^{4+}, and Ti^{4+} (0.71, 0.69, and 0.61 Å, respectively) were used.[46]

As listed in Table S1, the t and u values for the pure $SrZrS_3$ system are 0.856 and 0.391, respectively, indicating that the material can form a distorted perovskite structure. However, owing to the low u value, there is a high tendency for the needle-like NH_4CdCl_3 structure (*i.e.*, α-$SrZrS_3$) to form, which explains why $SrZrS_3$ exists in both needle-like and distorted perovskite structures. Because Zr^{4+} is larger than Hf^{4+}, Sn^{4+}, and Ti^{4+}, the substitution of Zr with Hf, Sn, or Ti atoms results in an increase in the t value, which increases linearly with the doping concentration. The highest increase in t was recorded for the Ti-based systems, followed by the Sn-based systems, which agrees well with the decreasing order of their ionic radii. The u-value, on the other hand, decreased monotonically with increasing doping concentration. The $SrZr_{0.5}Ti_{0.5}S_3$ recorded the lowest u-value of 0.360. According to Tiwari *et al.*, materials with u values in the range of 0.36 to 0.39 can be stabilized using mixed B cations or X anions.[50] Therefore, the t and u values of all the doped systems are within the appropriate range for the formation of distorted perovskite structures. However, with increasing doping concentration, the tendency to form needle-like structures increases.

3.2.2. Electronic properties of doped $SrZrS_3$. The electronic properties of semiconductor materials play a critical role in determining their suitability for optoelectronic applications. Such properties include the band structure, bandgap energy, nature of bandgap (direct *vs.* indirect), orientation of electronic states with respect to energy, DOS, and the contributions of different orbitals of the constituent atoms to the total DOS. In this study, our primary aim is to tune the bandgap of both phases of $SrZrS_3$ to values suitable for PV applications through substitutional doping with isovalent elements (Hf, Sn, and Ti) at the Zr site. We performed band structure and DOS calculations using the HSE06 functional to determine the bandgaps and other electronic properties of the doped $SrZrS_3$ systems.

Shown in Fig. 3 and Fig. S3 are the band structures of the $SrZr_{1-x}Hf_xS_3$, $SrZr_{1-x}Sn_xS_3$, and $SrZr_{1-x}Ti_xS_3$ systems, and Table 1 lists their band gaps, VBM, and CBM. For both α- and β-$SrZrS_3$, the substitution of Zr with Hf showed a negligible effect on the bandgap. The band gaps of both phases increased monotonically as the doping concentration increased from 0 to 50 atom% (*i.e.*, $x = 0.5$). With 50% replacement of Zr atoms, the band gaps of α- and β-$SrZrS_3$ increased by only 2.95% and 5.33%, respectively. The band structures show that for all x values, the $SrZr_{1-x}Hf_xS_3$ systems in both the α- and β-phases maintained a direct bandgap, with the VBM and CBM located at the Γ high symmetry point. Both the VBM and CBM were observed to shift to lower energies as x increased from 0.0 to 0.50 (Table 1). Analyses of the PDOS (Fig. 4 and Fig. S4) revealed that, similar to the pristine systems, the valence band (VB) and conduction band (CB) edges of both α- and β-$SrZr_{1-x}Hf_xS_3$ are dominated by the S-p and Zr-d orbitals, respectively, with the Hf-d orbital contributing negligibly to both VB and CB, which increased slightly with the increasing doping concentration.

For the $SrZr_{1-x}Sn_xS_3$ systems, a significant decrease in bandgap was observed in both α- and β-phases compared with that of the pristine systems. With the replacement of only 12.5% Zr atoms, the bandgap of α-$SrZrS_3$ decreased by 5.26% (from 1.56 to 1.48 eV), and that of β-$SrZrS_3$ decreased by 9.72% (from 2.03 to 1.83 eV). With a further increase in dopant concentration to 25%, the band gaps of both phases decreased; however, they increased again at higher dopant concentrations.

For both phases, the CB and VB of the Sn-doped systems are dominated by the S-p and Zr-d orbitals, respectively (Fig. 4 and Fig. S4). However, the Sn-s orbital contributes significantly to the edge of the CB, increasing band overlap and lowering the CBM, resulting in a decrease in the bandgap. These results are consistent with those reported for Sn-doped $BaZrS_3$, where a decrease in bandgap from 1.55 to 0.96 eV was recorded as 25% of the Zr atoms were replaced with Sn atoms.[55] According to the

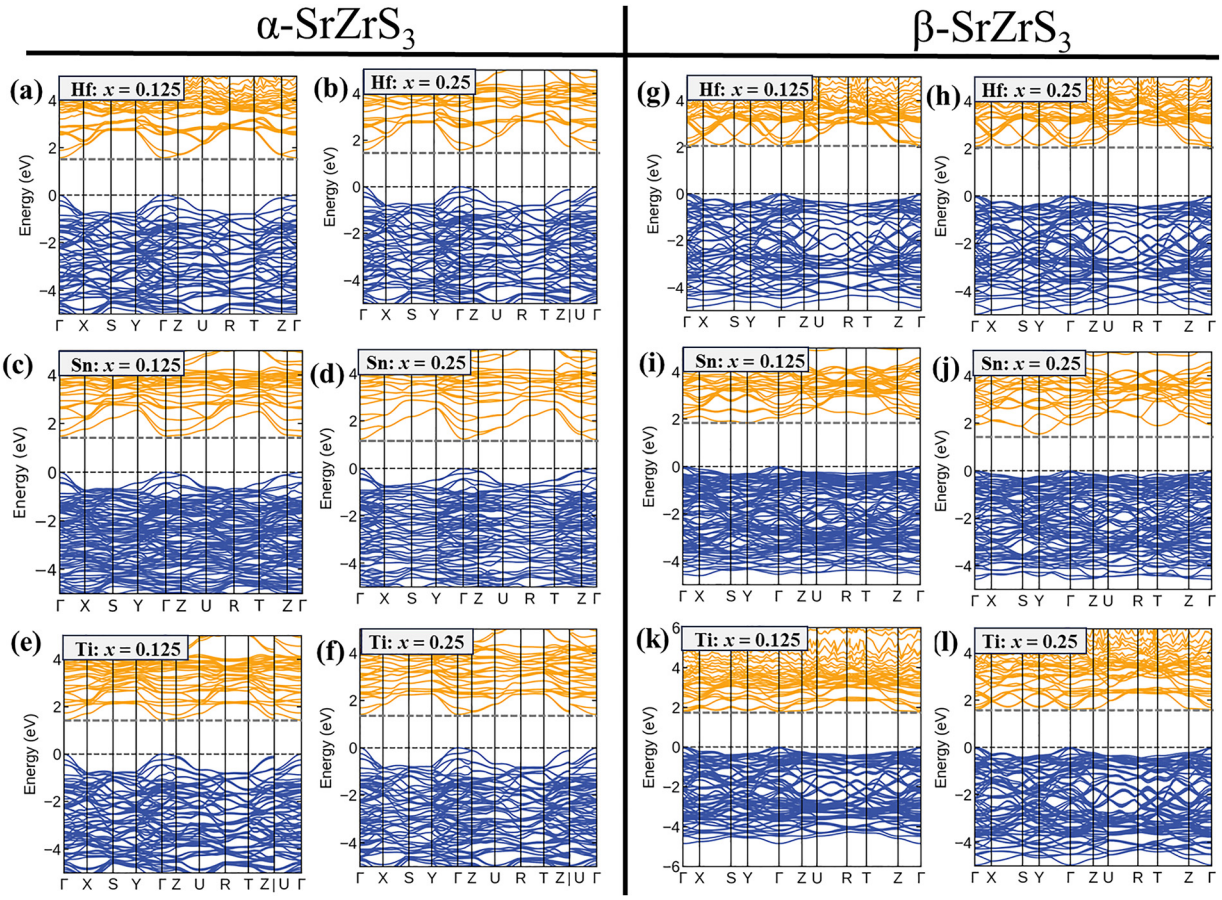

Fig. 3 Electronic band structures of (a–f) α- and (g–l) β-phase $SrZr_{1-x}Hf_xS_3$, $SrZr_{1-x}Sn_xS_3$, and $SrZr_{1-x}Ti_xS_3$ (x = 0.125 and 0.25) materials.

Table 1 Band gaps, valence band maximum (VBM), and conduction band minimum (CBM) of α- and β-$SrZr_{1-x}Hf_xS_3$, $SrZr_{1-x}Sn_xS_3$, and $SrZr_{1-x}Ti_xS_3$

	α-$SrZrS_3$			β-$SrZrS_3$		
System	Bandgap (eV)	VBM (eV)	CBM (eV)	Bandgap (eV)	VBM (eV)	CBM (eV)
$SrZrS_3$	1.56	4.02	5.58	2.03	3.31	5.34
$SrZr_{0.875}Hf_{0.125}S_3$	1.57	3.93	5.50	2.05	3.22	5.27
$SrZr_{0.75}Hf_{0.25}S_3$	1.58	3.83	5.41	2.07	3.13	5.20
$SrZr_{0.625}Hf_{0.375}S_3$	1.59	3.73	5.32	2.10	3.04	5.14
$SrZr_{0.50}Hf_{0.50}S_3$	1.61	3.63	5.24	2.14	2.95	5.08
$SrZr_{0.875}Sn_{0.125}S_3$	1.48	3.98	5.46	1.83/2.04	3.28	5.11
$SrZr_{0.75}Sn_{0.25}S_3$	1.20	3.97	5.17	1.54/1.78	3.22	4.77
$SrZr_{0.625}Sn_{0.375}S_3$	1.24	3.95	5.19	1.54/1.62	3.19	4.77
$SrZr_{0.50}Sn_{0.50}S_3$	1.30	3.87	5.17	1.44/1.48	3.15	4.59
$SrZr_{0.875}Ti_{0.125}S_3$	1.43	4.01	5.44	1.77	3.38	5.15
$SrZr_{0.75}Ti_{0.25}S_3$	1.41	4.12	5.52	1.59	3.44	5.03
$SrZr_{0.625}Ti_{0.375}S_3$	1.35	4.16	5.51	1.79	3.38	5.17
$SrZr_{0.50}Ti_{0.50}S_3$	1.29	4.20	5.49	1.70	3.44	5.14

authors, the decrease in the bandgap of the Sn-doped $BaZrS_3$ system is attributed to the higher electronegativity of Sn than Zr, resulting in short covalent bonds between Sn-s and S-p orbitals. In addition, the contribution of the Sn-s orbitals to the CB edge can enhance charge-carrier transport in the material, which is beneficial for PV applications.[55] Notably, indirect band gaps were observed for the β-$SrZr_{1-x}Sn_xS_3$ systems, suggesting that solar cells fabricated with these indirect bandgap materials need to be thicker to provide more opportunities for photo-emission and transition to take place. Compared to direct bandgap materials, the formation of an indirect bandgap for the β-$SrZr_{1-x}Sn_xS_3$ systems could result in lower light absorption efficiency, a large recombination lifetime, and therefore a considerable diffusion length.[56,57]

Ti doping showed a favorable decrease in the band gaps of both α- and β-$SrZrS_3$. With a doping concentration of 12.5%,

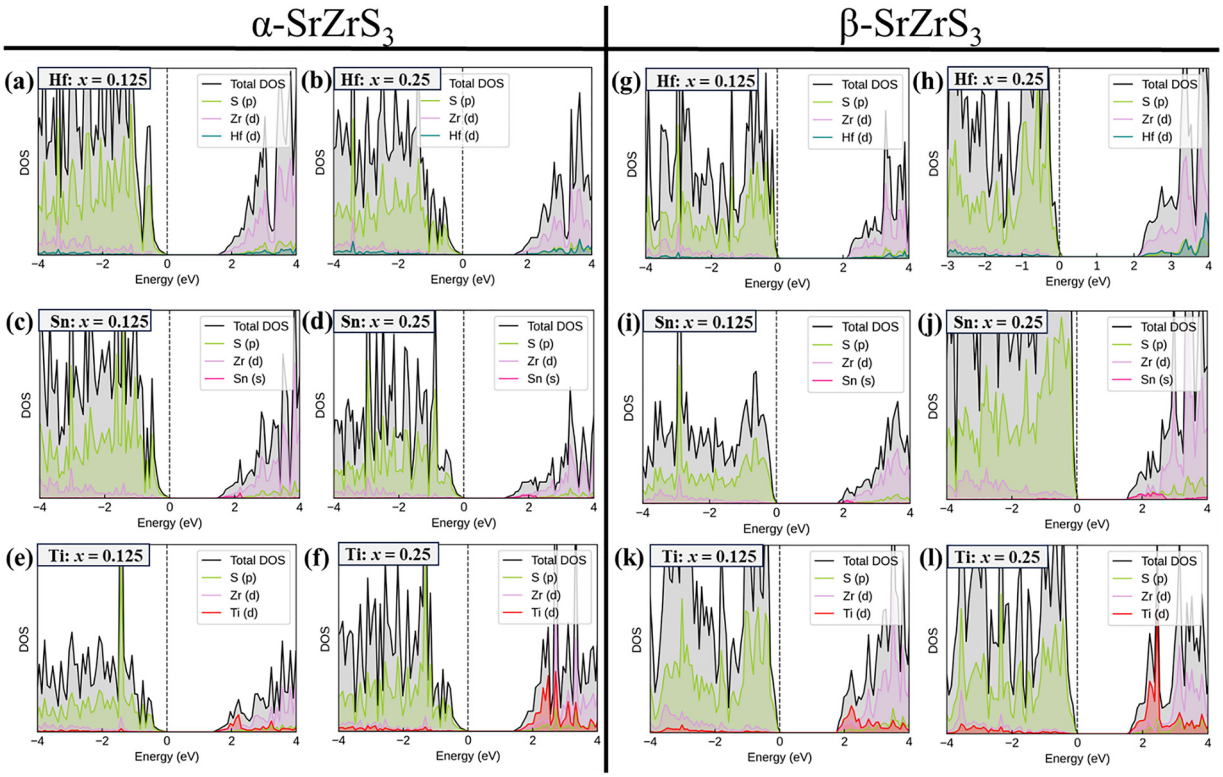

Fig. 4 Projected density of states (PDOS) of (a–f) α- and (g–l) β-phase $SrZr_{1-x}Hf_xS_3$, $SrZr_{1-x}Sn_xS_3$, and $SrZr_{1-x}Ti_xS_3$ (x = 0.125 and 0.25).

the bandgap of α-$SrZrS_3$ decreased to 1.43 eV, which is close to the optimum range for SJSCs. With a further increase in doping concentration, the bandgap decreased monotonically, reaching 1.35 eV at 37.5%. A similar trend was observed for β-$SrZrS_3$. However, beyond 25% doping, the bandgap of β-$SrZr_{1-x}Ti_xS_3$ increased with increasing doping concentration. The overall decrease in band gaps (compared to that of the pristine materials) recorded for α- and β-$SrZr_{1-x}Ti_xS_3$ is attributed to the lower energy of the Ti-3d orbital than that of the Zr-4d orbital.[30,48] As a result, the Ti-d orbital dominates the band edge of the CB, as revealed by the PDOS (Fig. 4 and Fig. S4), resulting in the lowering of the CBM (Table 1). These results agree well with previous DFT results reported for Ti-doped $BaZrS_3$.[48] Khan *et al.* also reported a lowering of the CB edge of Ti-doped $MAPbBr_3$, resulting in a decrease in the bandgap energy.[58] Therefore, Ti-doping is effective in lowering the bandgap energy of perovskite materials.

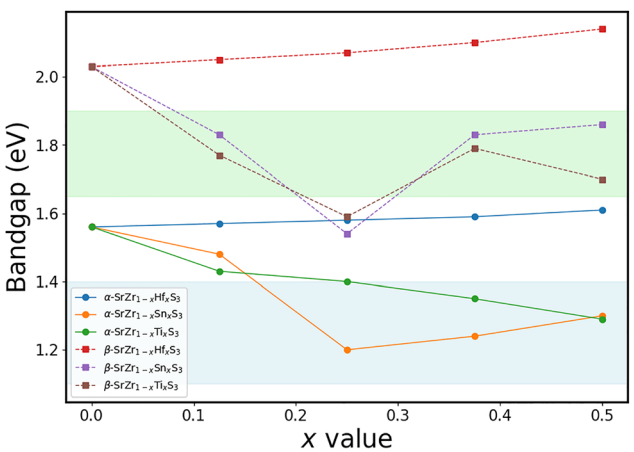

Fig. 5 Variation of the band gaps of α- and β-$SrZr_{1-x}Hf_xS_3$, $SrZr_{1-x}Sn_xS_3$, and $SrZr_{1-x}Ti_xS_3$ with the doping concentration x.

Fig. 5 summarizes the band gaps of the pristine and doped $SrZrS_3$ systems. The blue- and green-shaded regions indicate the optimum bandgap ranges for the maximum efficiency of SJSCs (1.10–1.40 eV) and TSCs (1.65–1.90 eV), respectively.[13,15,23,24] The band gaps of α-$SrZr_{1-x}Sn_xS_3$ and α-$SrZr_{1-x}Ti_xS_3$ with x values up to 0.25 lie well within the optimum range for SJSCs. Although the bandgap of α-$SrZr_{0.875}Ti_{0.125}S_3$ lies slightly above this range, the value is sufficient to yield a power conversion efficiency of up to 30% in SJSCs.[23] Furthermore, except for an x value of 0.25, the band gaps of β-$SrZr_{1-x}Sn_xS_3$ and β-$SrZr_{1-x}Ti_xS_3$ lie within the optimum range for the maximum performance of perovskite-based TSCs. According to the theoretical efficiency limit for Si/perovskite TSCs, considering a bandgap of 1.1 eV for Si, the ideal bandgap of a top perovskite cell is approximately 1.73 eV,[13] which is very close to 1.70 recorded for β-$SrZr_{0.5}Ti_{0.5}S_3$. For the Hf-doped systems, the band gaps for all doping concentrations lie outside the optimum range for both SJSCs and TSCs. However, at a high doping concentration, the α-$SrZr_{1-x}Hf_xS_3$ may be considered a top layer for TSCs, especially perovskite/perovskite TSCs.

Effective masses of holes (m_h^*) and electrons (m_e^*) in the vicinity of the Fermi level are also vital properties of PV materials as they play a key role in determining the charge transport characteristics in the material. The mobility of photo-generated electron–hole pairs, which highly influences the photoactivity of a material, is dependent on m_h^* and m_e^*, as shown in the following equation:[59,60]

$$\mu = e\frac{\tau}{m_{e(h)}^*}, \quad (8)$$

where e and τ are the electric charge and mean free path of an electron, respectively. This shows that effective masses are inversely related to the carrier mobility; therefore, low effective masses are desirable for PV applications.

The hole and electron effective masses are determined by the dispersion of the VB and CB edges of the band structures. They are inversely proportional to the curvature of the corresponding valence and conductance bands and can be expressed as follows:[59,61]

$$m_{e(h)}^* = \pm\hbar^2\left(\frac{d^2E_k}{dk^2}\right)^{-1}, \quad (9)$$

where E_k is the energy of an electron at wavevector k in that band, and $\hbar$ is the reduced Planck's constant. The term in the parenthesis can be obtained by fitting the energy of the conduction or valence band edges to a polynomial function. Herein, the effective masses were calculated from the band structures using SUMO software, and a k-points sampling of 3 was adopted for the polynomial fitting.[43]

Table S2 lists the calculated hole and electron effective masses along the Γ–X, Γ–Y, and Γ–Z, and Γ–Z high symmetry directions in the Brillouin zone. Pristine α-$SrZrS_3$ exhibits low m_h^* and m_e^* in the Γ–X and Γ–Y directions but high m_h^* and m_e^* in the Γ–Z, indicating higher carrier mobility in Γ–X and Γ–Y directions. The pristine β-$SrZrS_3$, on the other hand, exhibited m_h^* and m_e^* less than 1 in the three directions. The calculated values are comparable to those reported by Xue *et al.* for β-$SrZrS_3$.[31] For α-$SrZrS_3$, Hf doping reduced m_h^* in the Γ–X and Γ–Z directions but increased it in the Γ–Y direction, whereas the m_e^* in the Γ–X and Γ–Y directions decreased with increasing doping concentrations, but that in the Γ–Z direction increased. A similar trend was observed for the β-phase, where m_h^* and m_e^* in all the Γ–X and Γ–Y directions decreased but those in the Γ–Z direction increased with increasing doping concentrations. Considering the Sn-doped systems, both m_h^* and m_e^* in the three directions generally increased, indicating a decrease in both hole and electron mobility in Sn-doped $SrZrS_3$. Ti doping reduced the m_h^* of both α- and β-$SrZrS_3$ in the Γ–X and Γ–Y directions in but increased it in the Γ–Z direction. On the other hand, for both phases, m_e^* in the three directions increased with Ti doping. This indicates that Ti doping may enhance hole mobility but reduce electron mobility in α- and β-$SrZrS_3$.

To gain insight into the recombination rate of charge carriers, we calculated the ratios of m_h^* to m_e^* (denoted here as D in Table S2) in the Γ–X, Γ–Y, and Γ–Z directions. A high value of D indicates a greater difference between the hole and electron mobilities, resulting in the low recombination of electron–hole pairs.[62] For both the pristine and doped α-$SrZrS_3$, low D values were generally recorded in the Γ–X direction, whereas the relatively high D values were observed in the Γ–Y and Γ–Z directions. Conversely, for the β-phase, low D values were observed in the Γ–Z direction, whereas higher values were obtained in the Γ–X and Γ–Y directions. These results show that high charge-carrier recombination is expected in the Γ–X and Γ–Z high symmetry directions of α- and β-$SrZrS_3$, respectively.

3.2.3. Optical properties. The optical properties determine how a material interacts with incident light. Therefore, we determined the optical properties, including the dielectric functions, adsorption coefficient, reflectivity, refractivity, and energy loss function, of the pristine and doped $SrZrS_3$.

The dielectric function $\varepsilon(\omega)$, which comprises the real (ε_1) and imaginary (ε_2) parts, is a vital property because other optical properties of a material are determined from it. The imaginary part of the dielectric function indicates the radiation absorbed by the material, and the real part indicates the energy gain due to the scattering of the incident light.[55] The imaginary part also describes the absorptive behavior of a material, whereas the real part describes the degree of polarization.[63,64] A high dielectric constant is desired in PV applications as it promotes effective charge screening and decreases charge-carrier recombination.[60] Fig. 6 shows the real and imaginary parts of the dielectric function of the pristine and doped α- and β-$SrZrS_3$, and Fig. S6 shows the variation of their static dielectric functions with x values. The calculated static dielectric constant of the pristine α-$SrZrS_3$ is approximately 6.42. Substituting one Zr atom with Hf, this value first increased to approximately 7.13 (Fig. 6a). However, with a further increase in the doping concentration, the dielectric constant slightly decreased, with $SrZr_{0.5}Hf_{0.5}S_3$ exhibiting a dielectric constant of approximately 7.04. Sn-doping generally increased the static dielectric function of pristine α-$SrZrS_3$; however, the value tends to decrease at higher doping concentration (Fig. 6b). For Ti-doped α-$SrZrS_3$, with the substitution of 12.5% of the Zr atoms with Ti (*i.e.*, $x = 0.125$), the static dielectric function first slightly decreased (from 6.42 to 6.40). However, as the doping concentration further increased, the static dielectric function increased monotonically, reaching a value of 7.92 at an x value of 0.50 (Fig. 6c). Considering the imaginary part of the dielectric function, the main peak for the $SrZr_{1-x}Hf_xS_3$ system increased significantly at a photon energy of approximately 4 eV (Fig. 6d), indicating increased absorption of radiation. For the $SrZr_{1-x}Sn_xS_3$ and $SrZr_{1-x}Ti_xS_3$ systems, in addition to the increase in the peak intensity, the peaks were red-shifted, which corresponds to the decrease in the bandgap energies (Fig. 6(e) and (f)).

For the β-phase, the static dielectric function of $SrZr_{1-x}Hf_xS_3$ decreased monotonically from 7.78 to approximately 7.28 as the doping concentration increased from 0% to 50% (Fig. 6g). A similar result was observed for the β-$SrZr_{1-x}Sn_xS_3$ system, with the static dielectric function decreasing from 7.78 to 7.24

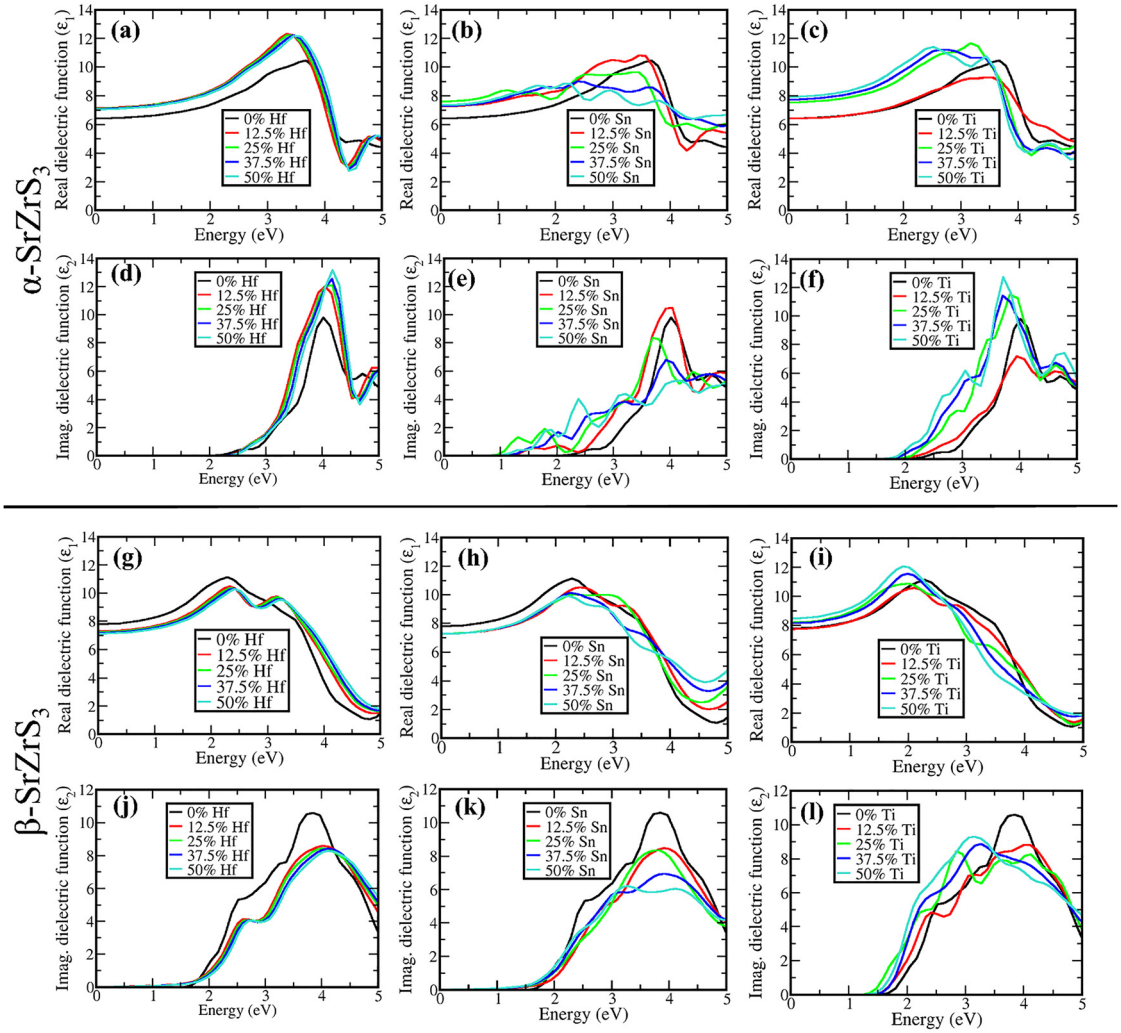

Fig. 6 Real and imaginary parts of the dielectric functions of (a–f) α- and (g–l) β-phase $SrZr_{1-x}Hf_xS_3$, $SrZr_{1-x}Sn_xS_3$, and $SrZr_{1-x}Ti_xS_3$.

as x increased from 0 to 0.5 (Fig. 6h). Doping with Ti also generally increased the dielectric constant of β-$SrZr_{1-x}Ti_xS_3$, except for the case of x = 0.25, where a slight decrease in the dielectric constant was observed (Fig. 6i). The reduction in the dielectric constant of β-$SrZr_{1-x}Sn_xS_3$ is consistent with the results reported for Sn-doped $BaZrS_3$ in the distorted perovskite structure.[48,55] Considering the imaginary part of the dielectric function, Hf and Sn doping generally shifted the region at which the material starts to absorb radiation to lower energies (red-shift) and significantly decreased the intensity of the main peak (Fig. 6j and k). The imaginary dielectric function of the β-$SrZr_{1-x}Ti_xS_3$ were also red-shifted, but the intensities of the peaks were higher than that of the pristine materials, except in the energy range of approximately 3.5–4.5 eV, where the intensity of the pristine material is significantly higher than that of the doped systems.

From the dielectric constants, we simulated other optical properties of the pristine and doped $SrZrS_3$ systems, including the absorption coefficient, energy loss function, reflectivity, and refractivity spectra in the visible range. The absorption coefficient measures how far light of a specific wavelength can penetrate a material before being absorbed, thereby determining the light-harvesting power of a material.[26,65] A high absorption coefficient results in a small diffusion length, making it possible to achieve high power conversion efficiency using a thin absorber layer (<1 μm).[21] Fig. 7 shows the absorption coefficients of the pristine and doped α- and β-$SrZrS_3$. Hf doping blue-shifted the absorption edge of both materials. It also increased the absorption of α-$SrZrS_3$ significantly in the energy range of approximately 3.5 to 4.3 eV (Fig. 7a). The main absorption peak of α-$SrZrS_3$ reached a maximum intensity of approximately 6.5 × 10^5 cm^{-1} at 4.2 eV, whereas those of α-$SrZr_{1-x}Hf_xS_3$ reached a maximum value of 8.64 × 10^5 cm^{-1} (for x = 0.5). However, further into the UV range (above photon energy of 4.5 eV), the absorption coefficients of the α-$SrZr_{1-x}Hf_xS_3$ decreased below that of the pristine material. The absorption spectra of the α-$SrZr_{1-x}Sn_xS_3$ and α-$SrZr_{1-x}Ti_xS_3$ systems also increased, but less significantly than that of α-$SrZr_{1-x}Hf_xS_3$. The two systems, especially at x values up to 0.25, start to absorb photons at energies much lower than that

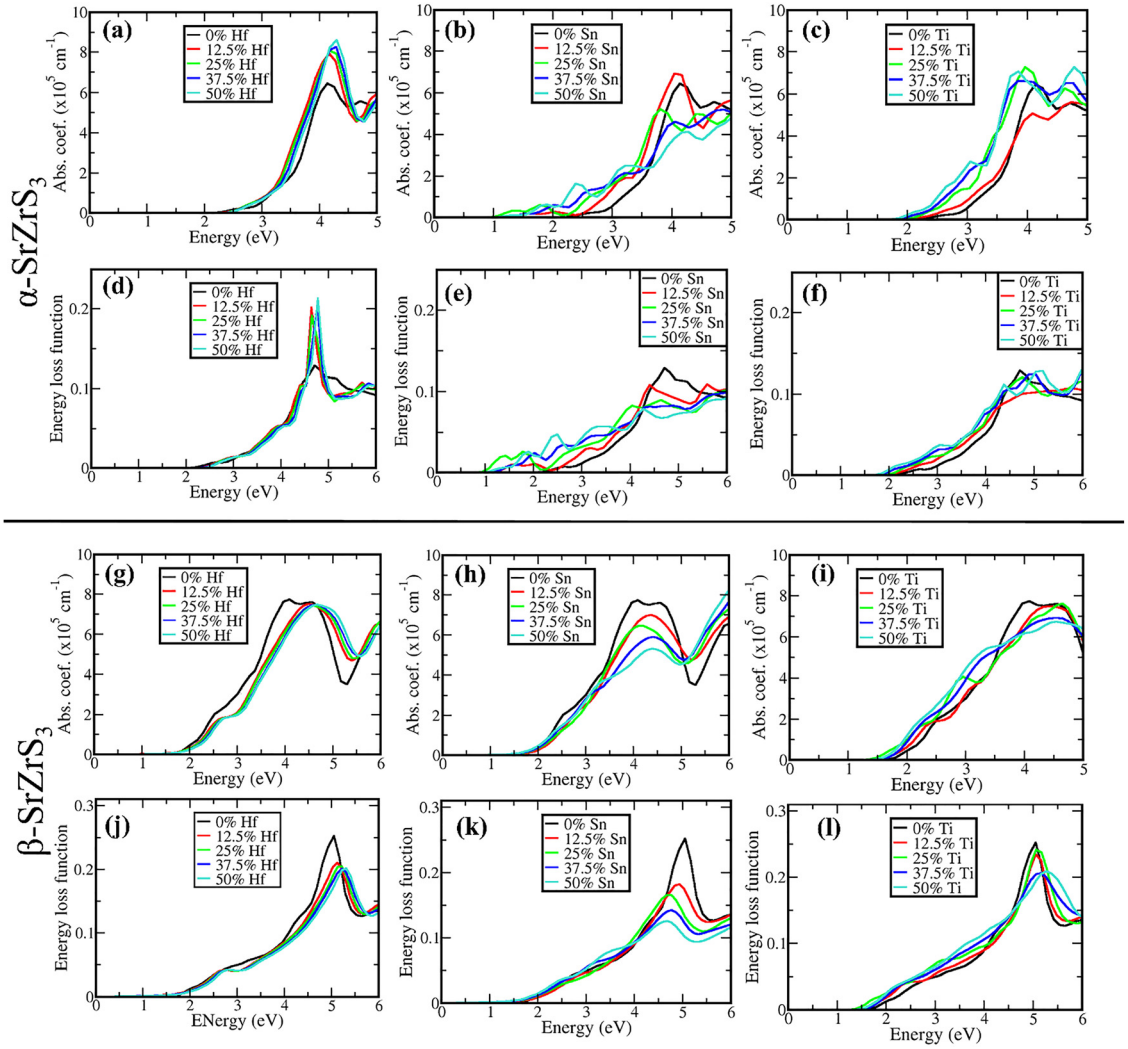

Fig. 7 Absorption coefficient and energy loss functions of (a–f) α- and (g–l) β-phase $SrZr_{1-x}Hf_xS_3$, $SrZr_{1-x}Sn_xS_3$, and $SrZr_{1-x}Ti_xS_3$.

of the pristine α-$SrZrS_3$, which corresponds to their reduced band gaps. α-$SrZr_{0.875}Sn_{0.125}S_3$ and α-$SrZr_{0.75}Ti_{0.25}S_3$ recorded maximum absorbance of 6.9 × 10^5 and 7.3 × 10^5 cm^{-1} at photon energies of approximately 4.1 and 3.9 eV, respectively.

For the β-$SrZrS_3$ systems, the three dopants generally reduced the absorption spectra of the material. In agreement with their increased band gaps, the commencement of absorption for β-$SrZr_{1-x}Hf_xS_3$ blue-shifted, whereas that for $SrZr_{1-x}Sn_xS_3$ and $SrZr_{1-x}Ti_xS_3$ red-shifted, which is consistent with their lower band gaps. For all *x* values, the intensity of the main peak of the pristine material remained higher than that $SrZr_{1-x}Hf_xS_3$ and $SrZr_{1-x}Sn_xS_3$ in the lower energy range. On the other hand, the intensity of the Ti-doped system was higher than that of the pristine material in the lower energy range. These results show that Hf and Sn doping improve the absorption spectra of α-$SrZrS_3$ but reduce that of β-$SrZrS_3$, whereas Ti doping improves the absorption spectra of both phases.

Fig. 7(d)–(f) and (j)–(l) show the energy loss functions of the α- and β-$SrZrS_3$ systems with and without dopants. The energy loss function represents the energy loss of fast electrons as they traverse a material.[63] For the α-phase, Hf doping significantly increased the energy loss spectra in the energy range of 4.4–5.0 eV, indicating an increase in energy loss of fast electrons in the Hf-doped material. On the other hand, Sn and Ti doping only slightly increased the energy loss spectra in the entire energy range, indicating that both dopants slightly increase the energy loss of fast electrons traversing through the material. For the β-phase, the three dopants, especially Hf and Sn, reduced the energy loss spectra of the material, thereby improving its performance in PV applications.

The reflectivity of a material is also an essential property to consider when evaluating it for PV applications. It measures the amount of incident photons lost to reflection. Lower reflectivity indicates a lower loss of photons, which is desirable for PV absorber layers. Fig. S5 shows the reflectivity of the pristine and doped α- and β-$SrZrS_3$. Hf and Sn doping generally increased the reflectivity of the α-phase in the low photon-energy range (Fig. S5a and b). The static reflectivity of α-$SrZr_{1-x}Hf_xS_3$ increased from approximately 0.188 to 0.206 as the *x* increased from 0 to 0.125 (Fig. S5a). With a further increase in *x*, the static

reflectivity decreased slightly, reaching a value of 0.204 at x = 0.50. However, for all x values, the reflectivity of α-$SrZr_{1-x}Hf_xS_3$ remained higher than that of the pristine material in the infrared and visible regions. The reflectivity significantly increased in the ultraviolet region (3.8–4.4 eV), reaching a maximum value of approximately 0.39 at an energy value of 4.17 eV (for $SrZr_{0.875}Hf_{0.125}S_3$). For the Sn-doped system, α-$SrZr_{0.75}Sn_{0.25}S_3$ recorded the highest static reflectivity of 0.22, which is 0.032 higher than that of the pure α-$SrZrS_3$ (Fig. S5b). The Ti-doped material showed a slight decrease in reflectivity in the entire plotted energy range when one Zr atom was replaced with a Ti atom (*i.e.*, x = 0.125); however, as doping concentration increased from 0.125 to 0.50, the reflectivity increased monotonously, $SrZr_{0.5}Ti_{0.5}S_3$ exhibiting the highest static reflectivity of 0.22 (Fig. S5c). These systems maintained high reflectivity across the entire infrared and visible regions; however, their reflectivity decreased below that of the pristine material at energy values exceeding 3.8 eV. For the β-phase, Hf and Sn doping showed a monotone decrease in reflectivity in the infrared and visible regions, $SrZr_{0.5}Hf_{0.5}S_3$ and $SrZr_{0.5}Sn_{0.5}S_3$ recording static reflectivity values of 0.206 and 0.210 (Fig. S5g and h), which are 0.017 and 0.013 lower than that of the pristine material (0.223), respectively. On the other hand, similar to the case of α-$SrZrS_3$, the reflectivity of β-$SrZrS_3$ first slightly decreased as the Ti-doping concentration increased from 0 to 0.125, after which it increased with further increase in x (Fig. S5i). These results show that Hf and Sn doping generally reduce the reflectivity of β-$SrZrS_3$ but increase that of α-$SrZrS_3$, whereas Ti reduces the reflectivity of both $SrZrS_3$ phases at low doping concentrations but increases it at high doping concentrations.

Fig. S5(d–f) and (j–l) show the refractive spectra of the undoped and doped $SrZrS_3$, which measure the degree to which photons are slowed down in the materials due to their interactions with electrons and other factors.[63] Low refractive indices indicate low photon diffraction in a material, which is beneficial in PV applications. For both phases and the three dopants, the refractive spectra followed the same trend as the reflectivity. Hf and Sn increased the refractivity of the α-phase but reduced that of the β-phase, whereas Ti doping reduced the refractivity of both phases at low concentrations but increased it at higher concentrations. These results indicate that Hf and Sn doping generally enhance the absorption coefficient of α-SrZrS3; however, they also increase its energy loss, reflectivity, and refractivity. In contrast, the two dopants reduce the energy loss, reflectivity, and refractivity of β-$SrZrS_3$ as well as the absorption coefficient. On the other hand, Ti doping increases the absorption coefficient and energy function of α-$SrZrS_3$ and slightly lowers those of β-$SrZrS_3$. However, for both phases, it lowers the reflectivity and refractive spectra only at a low doping concentration.

3.2.4. Thermodynamic stability. In predicting materials for solar applications, thermodynamic stability is a crucial consideration because it indicates the ability to synthesize the material under equilibrium conditions.[66] In addition, thermodynamically stable materials pose fewer technological challenges when incorporated into devices.[67] Therefore, it is vital to determine the thermodynamic stability of the pristine as well as doped $SrZrS_3$.

During the synthesis of ternary systems like $SrZrS_3$, the formation of elemental (Sr, Zr, and S) and binary (such as SrS, SrS_2, and ZrS) phases always competes with the desired ternary phase. In addition to these, ternary and possibly quaternary phases could compete with the formation of quaternary systems, such as $SrZr_{1-x}Hf_xS_3$, $SrZr_{1-x}Sn_xS_3$, and $SrZr_{1-x}Ti_xS_3$. This competition can be quantitatively described by the limit to the chemical potentials of the component elements.[67] Chemical potentials represent the energy of the reservoirs with which atoms are exchanged.[68] They can be defined as the partial molar derivative of the Gibbs free energy with respect to elemental species. Under constant temperature and pressure, the chemical potential determines the stability of substances and their tendency to chemically react to form new substances, transform into new physical states, or migrate from one spatial location to another.[69] It is, therefore, necessary to predict the range of chemical potentials of the constituent elemental species of a material over which the target phase, rather than the elemental species or competing phases, is stable. This can be achieved by comparing the free energy of the material with that of all competing phases, including those consisting of subsets of the elemental species in the material.[70]

To synthesize a ternary-phase material with the chemical formula $A_xB_yC_z$ under equilibrium conditions, the chemical potential of the constituent elements (*i.e.*, μ_A, μ_B, and μ_C) in the synthesis environment must satisfy the following conditions:[67,71]

$$x\mu_A + y\mu_B + z\mu_C = \Delta H_{f(A_xB_yC_z)}, \quad (10)$$

where $\Delta H_{f(A_xB_yC_z)}$ is the formation enthalpy of the material. To avoid the precipitation of the elemental phases in the synthesis environment, μ_A, μ_B, and μ_C must be less than zero. Similarly, to avoid the formation of a binary phase A_nB_m, the following conditions must also be satisfied:[67]

$$m\mu_A + n\mu_B < \Delta H_{f(A_mB_n)}. \quad (11)$$

This applies to ternary or quaternary phases.

Herein, we considered the thermodynamic stability of $SrZrS_3$. We screened the Materials Project database to identify $SrZrS_3$ competing phases whose energies above Hull are less than 0.01 eV per atoms, which include the elemental phases (Sr, Zr, and S) and binary phases (SrS, SrS_3, ZrS, ZrS_2, ZrS_3, Zr_2S, Zr_3S_4, and Zr_9S_2). Therefore, based on eqn (11), stable $SrZrS_3$ can be synthesized without the formation of the competing phases if the following constraints are satisfied:

$$\mu_{Sr} < 0$$

$$\mu_{Zr} < 0$$

$$\mu_S < 0$$

$$\mu_{Sr} + \mu_S < \Delta H_{f(SrS)}$$

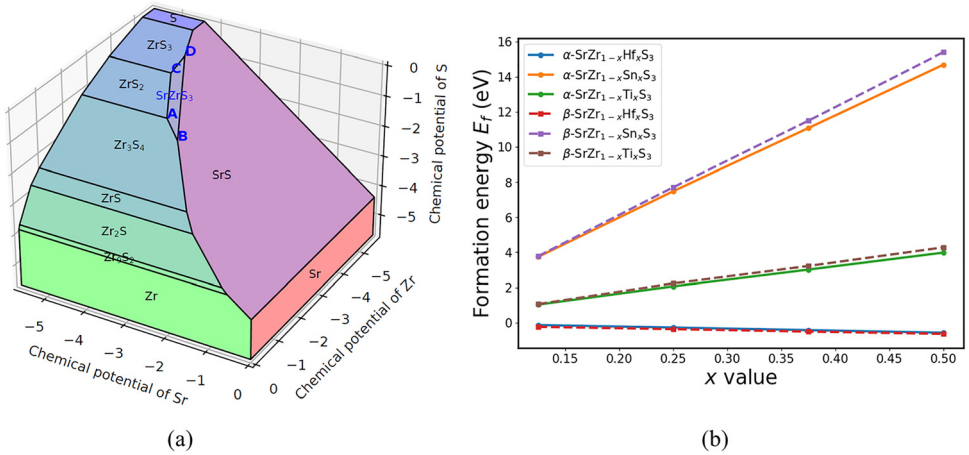

(a) (b)

Fig. 8 (a) Thermodynamically stable region of $SrZrS_3$ in the Sr–Zr–S system. (b) Substitutional defect formation energies of α- and β-$SrZr_{1-x}Hf_xS_3$, $SrZr_{1-x}Sn_xS_3$, and $SrZr_{1-x}Ti_xS_3$.

$$\mu_{Sr} + 3\mu_S < \Delta H_{f(SrS_3)}$$

$$\mu_{Zr} + \mu_S < \Delta H_{f(ZrS)}$$

$$\mu_{Zr} - 2\mu_S < \Delta H_{f(ZrS_2)}$$

$$\mu_{Zr} + 3\mu_S < \Delta H_{f(ZrS_3)}$$

$$2\mu_{Zr} + \mu_S < \Delta H_{f(Zr_2S)}$$

$$3\mu_{Zr} + 4\mu_S < \Delta H_{f(Zr_3S_4)}$$

$$9\mu_{Zr} + 2\mu_S < \Delta H_{f(Zr_9S_2)}$$

The enthalpies of formation (considered as the total energies per unit chemical formula) of the target and competing materials were calculated using the PBE functional, and the chemical potential diagram (Fig. 8(a)) was plotted using pydefect software.[72]

As shown in Fig. 8(a), the chemical stability window for $SrZrS_3$ is a trapezium bound by four coexistence curves AB, AC, BD, and CD, where $SrZrS_3$ coexists with Zr_3S_4, ZrS_2, SrS, and ZrS_3, respectively. This is consistent with the experimental study reported by Lee *et al.*, in which small amounts of ZrS_3, ZrS_2, and SrS were observed to coexist with β-$SrZrS_3$ synthesized *via* solid-state reactions.[20] Bystrický *et al.* also reported the coexistence of ZrS_2 and ZrO_2 with β-$SrZrS_3$ synthesized *via* the solid-state sulfurization of Sr and ZrO_2.[73] The vertices B and D represent Zr-rich/S-poor and S-poor/Zr-rich regions, respectively. Lines AB and CD also represent Zr-rich/S-poor and S-poor/Zr-rich regions, indicating that Zr_3S_4 and ZrS_3 could be precipitated under Zr-rich/S-poor and S-poor/Zr-rich conditions, respectively. On the other hand, lines AC and AC extend from Zr-rich/S-poor to S-poor/Zr-rich regions, indicating that the precipitation of SrS and ZrS_2 is not an indicator of the chemical potential limits of Zr and S.[74] Overall, this chemical potential diagram shows that $SrZrS_3$ is stable, which is consistent with previous experimental studies, where both $SrZrS_3$ phases have been successfully synthesized.[19,20,73,75] However, the stability window is narrow, indicating the need for adequate control of the synthesis environment to prevent the synthesis of the competing phases.

Next, to determine whether the doped systems can be synthesized, we calculated the defect formation of the dopants in $SrZrS_3$ using the supercell approach.[68] Based on this approach, the formation energy E_f of an intrinsic or extrinsic point defect X in a material can be calculated using the following formula:[76,77]

$$E_f = E_{tot}[X^q] - E_{tot}[\text{pure}] - \sum_i n_i\mu_i + q[E_F + E_v + \Delta V], \quad (12)$$

where $E_{tot}[X^q]$ is the total energy of the supercell containing defect X, $E_{tot}[\text{pure}]$ the total energy of the perfect crystal with the same supercell size, n_i the number of atoms of species i added to ($n_i > 1$) or removed from ($n_i < 1$) the supercell to form the defect, μ_i the chemical potentials of species i, and q the charge state of the defect. E_F is the Fermi energy level with reference to the VBM of the bulk material E_v, and ΔV is a correction term, which accounts for the difference between the reference potential in the supercell and that in the bulk. Herein, we assume that the doped systems $SrZr_{1-x}Hf_xS_3$, $SrZr_{1-x}Sn_xS_3$, and α-$SrZr_{1-x}Ti_xS_3$ are in the charge-neutral states; therefore, $q = 0$.

Fig. 8(b) and Table S3 show the formation energies of the $SrZr_{1-x}Hf_xS_3$, $SrZr_{1-x}Sn_xS_3$, and $SrZr_{1-x}Ti_xS_3$ systems in the α- and β-phases. For both phases, the formation energies of $SrZr_{1-x}Hf_xS_3$ were less than zero and decreased linearly with increasing x value, whereas those of $SrZr_{1-x}Sn_xS_3$ and $SrZr_{1-x}Ti_xS_3$ were greater than zero and increased linearly with x.

These results show that $SrZr_{1-x}Hf_xS_3$ can be synthesized through an exothermic process, whereas $SrZr_{1-x}Sn_xS_3$ or $SrZr_{1-x}Ti_xS_3$ can only be formed through endothermic processes. For $SrZr_{1-x}Hf_xS_3$, the defect formation energies of the β-phase are slightly lower than those of the α-phase for all x values, indicating that it is easier to dope Hf into β-$SrZrS_3$ than into α-$SrZrS_3$. In contrast, for all values of x, the calculated

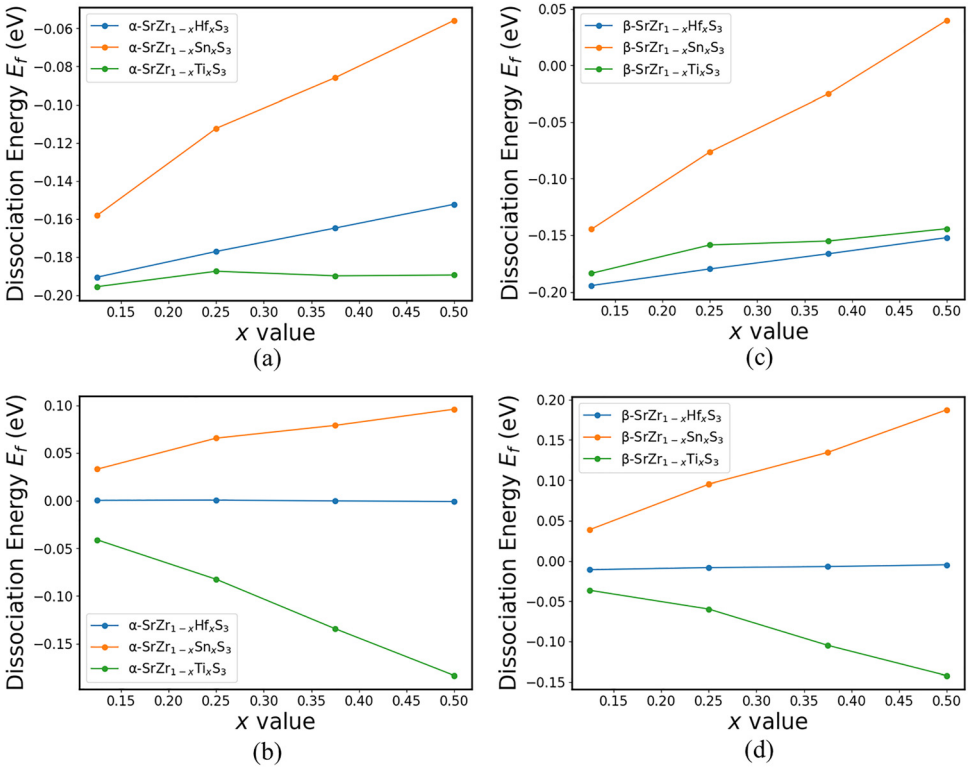

Fig. 9 Dissociation energies of (a) and (b) α-phases and (c) and (d) β-phases of $SrZr_{1-x}Hf_xS_3$, $SrZr_{1-x}Sn_xS_3$, and $SrZr_{1-x}Ti_xS_3$ into (a) and (c) binary phases and (b) and (d) ternary phases.

defect formation energies of $SrZr_{1-x}Sn_xS_3$ and $SrZr_{1-x}Ti_xS_3$ in the α-phase are lower than those in the β-phase, indicating than Sn and Ti doping of α-$SrZrS_3$ is more energetically favorable than that of β-$SrZrS_3$. The very high defect formation energies of the $SrZr_{1-x}Ti_xS_3$ systems indicate that high energy is required to dope $SrZrS_3$ with Sn at the Zr site.

To further determine the stability of the doped systems, we calculated the energies required for the systems to dissociate into secondary binary phases, such as SrS, ZrS_3, and MS_2 (M = Hf, Sn, or Ti), or ternary phases, such as $SrZrS_3$ and $SrMS_3$. The energy required to dissociate $SrZr_{1-x}M_xS_3$ into binary and ternary phases can be calculated as follows:[55]

$$E_d^b = xE_T(SrZr_{x-1}M_xS_3) - E_T(SrS) - (1-x)E_T(ZrS_2) - xE_T(MS_2), \quad (13)$$

$$E_d^T = E_T(SrZr_{x-1}M_xS_3) - (1-x)E_T(SrZrS_3) - xE_T(SrMS_3), \quad (14)$$

where E_d^b and E_d^T are the decomposition energies into binary and ternary secondary phases, respectively, and $E_T(X)$ is the calculated total energy of compound X in its most stable crystal structure.

Fig. 9 and Table S3 show the calculated dissociation energies of $SrZr_{1-x}Hf_xS_3$, $SrZr_{1-x}Sn_xS_3$, and $SrZr_{1-x}Ti_xS_3$ in both the α- and β-phases. For both phases, E_d^b for all the systems is less than zero, except for β-$SrZr_{0.5}Sn_{0.5}S_3$, where E_d^b is slightly greater than zero (0.0399 eV). This indicates that the dissociation of the doped systems into binary secondary phases is not thermodynamically favorable. As shown in Fig. 9(a) and (b), E_d^b increases nearly linearly with x, indicating that at higher doping concentrations, the systems become more susceptible to dissociation into binary phases. Considering the ternary dissociation (Fig. 9(a) and (b)), for all values of x, the E_d^T values of $SrZr_{1-x}Ti_xS_3$ in both phases are negative and decrease significantly with increasing x value, indicating that under equilibrium conditions, $SrZr_{1-x}Ti_xS_3$ is more stable than the competing ternary phases. In contrast, the dissociation energy of both α- and β-$SrZr_{1-x}Sn_xS_3$ is positive and increases with increasing x value, indicating its tendency to dissociate into the ternary phases under thermodynamic equilibrium conditions. For $SrZr_{1-x}Hf_xS_3$, the E_d^T values in both α- and β-phases are very close to zero. In the α-phase, it decreases from 0.0004 to −0.0007 eV as x increases from 0.125 to 0.50, indicating that the system would dissociate into ternary phases at low Hf doping concentrations. For the β-phase, the E_d^T values are all negative and slightly increase with the x value, indicating an increasing tendency to dissociate into ternary phases. These results show that Ti-doped $SrZrS_3$ is more stable than Hf- and Sn-doped $SrZrS_3$ under thermodynamic equilibrium conditions.

4. Summary and conclusion

In this study, we investigated the effect of Hf, Sn, and Ti doping on the structural, electronic, and optical properties of α- and β-$SrZrS_3$ through hybrid DFT calculations. For both α- and β-phases, we considered the three dopants at the Zr sites,

forming $SrZr_{1-x}Hf_xS_3$, $SrZr_{1-x}Sn_xS_3$, and $SrZr_{1-x}Ti_xS_3$, with x varying from 0.125 to 0.50. We found that Hf and Ti doping generally shrink the volumes of both α- and β-$SrZrS_3$, which is consistent with the smaller ionic radii of Hf^{4+} and Ti^{4+} compared to those of Zr^{4+}. In contrast, Sn doping expanded the α- and β-$SrZrS_3$ unit cells, although the radius of Sn^{4+} is smaller than that of Zr^{4+}. Structural stability analysis revealed that the three dopants reduce the ability of $SrZrS_3$ to form a perovskite structure as they lower the Goldschmidt tolerance and octahedral factors of the system. Band structure calculations revealed that Hf doping increases the band gaps of both α- and β-$SrZrS_3$, whereas Sn or Ti doping lowers the band gaps. With x values up to 0.25, the band gaps of α-$SrZr_{1-x}Sn_xS_3$ and α-$SrZr_{1-x}Ti_xS_3$, lie within the optimum range for SJSCs, and those of β-$SrZr_{1-x}Sn_xS_3$ and β-$SrZr_{1-x}Ti_xS_3$ are appropriate for Si/perovskite and perovskite/perovskite TSCs. Furthermore, Hf and Sn doping generally improved the absorption coefficient of α-$SrZrS_3$ but also increased its energy loss, reflectivity, and refractivity. In contrast, both dopants reduced the energy loss, reflectivity, and refractivity as well as the absorption coefficient of β-$SrZrS_3$. On the other hand, Ti doping increased the absorption coefficient and energy function of α-$SrZrS_3$ and slightly lowered those of β-$SrZrS_3$. Thermodynamic stability analysis revealed that $SrZr_{1-x}Hf_xS_3$ can be formed *via* an exothermic process, whereas $SrZr_{1-x}Sn_xS_3$ and $SrZr_{1-x}Ti_xS_3$ can only be synthesized *via* endothermic procedures. Further thermodynamic analysis showed that both α- and β-$SrZr_{1-x}Ti_xS_3$ are more stable than their binary and ternary competing phases, whereas the $SrZr_{1-x}Sn_xS_3$ systems are prone to dissociation into ternary phases under thermodynamic equilibrium conditions. These results show that although Ti and Sn are effective in lowering the band gaps of α- and β-$SrZrS_3$, Ti doping is more thermodynamically favorable, making it more promising for the bandgap engineering of $SrZrS_3$ for PV applications.

Conflicts of interest

There are no conflicts to declare.

Data availability

The data that support the findings of this study are available on request from the corresponding author.

Supplementary information (SI) contains the optimized structures, band structures, projected density of states (PDOS), optical spectra (reflectivity and refractivity), and a summary of structural parameters, effective masses, and formation energies of the α- and β-phases of $SrZr_{1-x}Hf_xS_3$, $SrZr_{1-x}Sn_xS_3$, and $SrZr_{1-x}Ti_xS_3$. See DOI: **https://doi.org/10.1039/d5cp02689j**.

Acknowledgements

This work was supported by the U.S. Department of Energy, Office of Science, Basic Energy Sciences, Early Career Program, under Award No. DOE DE-SC0025350. The authors also acknowledge the support of the College of Earth and Mineral Sciences and the John and Willie Leone Family Department of Energy and Mineral Engineering of Pennsylvania State University. Computations for this research were performed on the Pennsylvania State University's Institute for Computational and Data Sciences' Roar supercomputer and the National Computational Infrastructure (NCI Australia), enabled by the National Collaborative Research Infrastructure Strategy (NCRIS).[78]

References

1 H. Chen, C. Liu, J. Xu, A. Maxwell, W. Zhou, Y. Yang, Q. Zhou, A. Bati, H. Wan, Z. Wang, L. Zeng, J. Wang, P. Serles, Y. Liu, S. Teale, Y. Liu, M. Saidaminov, M. Li, N. Rolston, S. Hoogland, T. Filleter, M. G. Kanatzidis, B. Chen, Z. Ning and E. Sargent, *et al.*, *Science*, 2024, **384**, 189–193.
2 A. Kojima, K. Teshima, Y. Shirai and T. Miyasaka, *J. Am. Chem. Soc.*, 2009, **131**, 6050–6051.
3 W. Peng, J. Yin, K. Ho, O. Ouellette, M. De Bastiani, B. Murali, O. El Tall, C. Shen, X. Miao, J. Pan, E. Alarousu, J. He, B. Ooi, O. Mohammed, E. Sargent and O. Bakr, *Nano Lett.*, 2017, **17**, 4759–4767.
4 D. Shi, V. Adinolfi, R. Comin, M. Yuan, E. Alarousu, A. Buin, Y. Chen, S. Hoogland, A. Rothenberger, K. Katsiev, Y. Losovyj, X. Zhang, P. Dowben, O. Mohammed, E. Sargent and O. Bakr, *Science*, 2015, **347**, 519–522.
5 M. R. A. Elsayed, E. A. Mourtada, A. A. Abdelmageed, H. M. Hashem and A. Hassen, *Sci. Rep.*, 2023, **13**, 10115.
6 A. Faridi, M. Imran, G. Tariq, S. Ullah, S. Noor, S. Ansar and F. Sher, *Ind. Eng. Chem. Res.*, 2023, **62**, 4494–4502.
7 J. Zhang, C. Bai, Y. Dong, W. Shen, Q. Zhang, F. Huang, Y. Cheng and J. Zhong, *Chem. Eng. J.*, 2021, **425**, 131444.
8 N. Falsini, A. Ristori, F. Biccari, N. Calisi, G. Roini, P. Scardi, S. Caporali and A. Vinattieri, *J. Eur. Opt. Soc. – Rapid Publ.*, 2021, **17**, 1–7.
9 Z. Luo, C. Zhang, L. Yang and J. Zhang, *ChemSusChem*, 2022, **15**, e202102008.
10 M. Wang and C. J. Carmalt, *ACS Appl. Energy Mater.*, 2021, **5**, 5434–5448.
11 Y. Cheng and L. Ding, *SusMat*, 2021, **1**, 324–344.
12 J. Yang and Q. Bao, *Opt. Express*, 2024, **32**, 8614–8622.
13 Y. Shi, J. J. Berry and F. Zhang, *ACS Energy Lett.*, 2024, **9**, 1305–1330.
14 Interactive Best Research-Cell Efficiency Chart | Photovoltaic Research|NREL, **https://www.nrel.gov/pv/interactive-cell-efficiency.html** (accessed Sept. 20240).
15 R. Lin, Y. Wang, Q. Lu, B. Tang, J. Li, H. Gao, Y. Gao, H. Li, C. Ding, J. Wen, P. Wu, C. Liu, S. Zhao, K. Xiao, Z. Liu, C. Ma, Y. Deng, L. Li, F. Fan and H. Tan, *Nature*, 2023, **620**, 994–1000.
16 G. E. Eperon, T. Leijtens, K. Bush, R. Prasanna, T. Green, J. Wang, D. McMeekin, G. Volonakis, R. Milot, R. May, A. Palmstrom, D. Slotcavage, R. Belisle, J. Patel, E. Parrott, R. Sutton, W. Ma, F. Moghadam, B. Conings, A. Babayigit,

H. Boyen, S. Bent, F. Giustino, L. Herz, M. Johnston, M. McGehee and H. Snaith, *Science*, 2016, **354**, 861–865.
17 S. Perera, PhD Thesis, State University of New York, 2021.
18 S. Niu, J. Milam-Guerrero, Y. Zhou, K. Ye, B. Zhao, B. Melot and J. Ravichandran, *J. Mater. Res.*, 2018, **33**, 4135–4143.
19 N. Jaykhedkar, B. A. Roman, A. Milan and T. Bučko, *J. Mater. Chem. C*, 2022, **10**, 12032.
20 C. S. Lee, K. M. Kleinke and H. Kleinke, *Solid State Sci.*, 2005, **7**, 1049–1054.
21 Y. Sun, M. Agiorgousis, P. Zhang and S. Zhang, *Nano Lett.*, 2015, **15**, 581–585.
22 P. Basera and S. Bhattacharya, *J. Phys. Chem. Lett.*, 2022, **13**, 6439–6446.
23 S. Rühle, *Sol. Energy*, 2016, **130**, 139–147.
24 Single Junction Solar Cells Vs Multi-Junction Solar Cells, **https://g2voptics.com/photovoltaics-solar-cells/types-of-solar-cells/** (accessed Sept. 2024).
25 Y. Nishigaki, T. Nagai, M. Nishiwaki, T. Aizawa, M. Kozawa, K. Hanzawa, Y. Kato, H. Sai, H. Hiramatsu, H. Hosono and H. Fujiwara, *Solar RRL*, 2020, **4**, 1900555.
26 H. I. Eya, E. Ntsoenzok and N. Y. Dzade, *Materials*, 2020, **13**, 978.
27 C. He, J. Qiu, Z. Mu and X. Liu, *CCS Chem.*, 2023, **5**, 1961–1972.
28 W. Meng, B. Saparov, F. Hong, J. Wang, D. Mitzi and Y. Yan, *Chem. Mater.*, 2016, **28**, 821–829.
29 Z. Yu, C. Deng, S. Kong, H. Hui, J. Guo, Q. Zhao, F. Tian, C. Zhou, Y. Zhang, S. Yang and H. Zeng, *J. Magn. Magn. Mater.*, 2022, **563**, 169886.
30 X. Wei, H. Hui, S. Perera, A. Sheng, D. Watson, Y. Sun, Q. Jia, S. Zhang and H. Zeng, *ACS Omega*, 2020, **5**, 18579–18583.
31 Y. Xue, C. Lin, Y. Huang, S. Zhang, J. Zhong and D. Huang, *Phys. B*, 2023, **658**, 414839.
32 B. Xu, W. Wang, X. Zhang, W. Cao, D. Wu, S. Liu, H. Dai, S. Chen, K. Wang and X. Sun, *J. Mater. Chem. C*, 2017, **25**, 6123.
33 Y. Shi, J. Xi, T. Lei, F. Yuan, J. Dai, C. Ran, H. Dong, B. Jiao, X. Hou and Z. Wu, *ACS Appl. Mater. Interfaces*, 2018, **11**, 9849–9857.
34 A. Hazarika, *ACS Nano*, 2018, **12**, 49.
35 G. Nedelcu, *et al.*, *Nano Lett.*, 2015, **15**, 5635–5640.
36 G. Kresse, *J. Non-Cryst. Solids*, 1995, **192–193**, 222–229.
37 G. Kresse and J. Furthmüller, *Phys. Rev. B: Condens. Matter Mater. Phys.*, 1996, **54**, 11169–11186.
38 P. E. Blöchl, *Phys. Rev. B: Condens. Matter Mater. Phys.*, 1994, **50**, 17953–17979.
39 G. Kresse and D. Joubert, *Phys. Rev. B: Condens. Matter Mater. Phys.*, 1999, **59**, 1758–1775.
40 R. Lelieveld and D. J. W. IJdo, *Acta Crystallogr., Sect. B*, 1980, **36**, 2223–2226.
41 J. P. Perdew, M. Ernzerhof and K. Burke, *Phys. Rev. Lett.*, 1996, **77**, 3865–3868.
42 M. Kumar, A. Singh, D. Gill and S. Bhattacharya, *J. Phys. Chem. Lett.*, 2021, **12**, 5301–5307.
43 M. Ganose, A. J. Jackson and D. O. Scanlon, *J. Open Source Software*, 2018, **3**, 717.
44 V. Wang, N. Xu, J. C. Liu, G. Tang and W. T. Geng, *Comput. Phys. Commun.*, 2021, **267**, 108033.
45 S. Niu, H. Huyan, Y. Liu, M. Yeung, K. Ye, L. Blankemeier, T. Orvis, D. Sarkar, D. Singh, R. Kapadia and J. Ravichandran, *Adv. Mater.*, 2017, **29**, 1604733.
46 R. D. Shannon, *Acta Crystallogr.*, 1976, **32**, 751.
47 R. D. Shannon and C. T. Prewitt, *Acta Crystallogr., Sect. B*, 1969, **25**, 925–946.
48 M. B. Kanoun, B. U. Haq, A. A. Kanoun and S. Goumri-Said, *Energy Fuels*, 2023, **37**, 9548–9556.
49 Z. Xu, C. Zhang, Y. Wu, J. Gong, W. Wang, Z. Liu and H. Chen, *Results Phys.*, 2019, **15**, 102709.
50 D. Tiwari, O. S. Hutter and G. Longo, *JPhys Energy*, 2021, **3**, 034010.
51 C. Li, X. Lu, W. Ding, L. Feng, Y. Gao and Z. Guo, *Acta Crystallogr., Sect. B: Struct. Sci.*, 2008, **64**, 702–707.
52 M. R. Filip and F. Giustino, *Proc. Natl. Acad. Sci. U. S. A.*, 2018, **115**, 5397–5402.
53 S. Pereraa, H. Huia, C. Zhaoa, H. Xuea, F. Suna, C. Dengc, N. Grossa, C. Millevilled, X. Xuc, D. Watsond, B. Weinsteina, Y. Sune, S. Zhange and H. Zeng, *Nano Energy*, 2016, **22**, 129–135.
54 C. Comparotto, A. Davydova, T. Ericson, L. Riekehr, M. Moro, T. Kubart and J. Scragg, *ACS Appl. Energy Mater.*, 2020, **3**, 2762–2770.
55 R. Chami, A. Lekdadri, M. Chafi, L. H. Omari and E. K. Hlil, *Solid State Commun.*, 2023, **369**, 115212.
56 D. Liang and J. E. Bowers, *Nat. Photonics*, 2010, **4**, 511–517.
57 M. H. Miah, M. U. Khandaker, M. B. Rahman, M. Nur-E-Alam and M. A. Islam, *RSC Adv.*, 2024, **14**, 15876–15906.
58 M. Khan, S. Hussain, M. Saleem, F. Alzahrani, M. Siddique, M. Hassan, A. Khalid and M. Iqbal, *Phys. B*, 2024, **674**, 415575.
59 M. Dong, J. Zhang and J. Yu, *APL Mater.*, 2015, **3**, 104404.
60 N. Y. Dzade, *Sci. Rep.*, 2021, **11**, 4755.
61 G. Ozgur, **https://s2.smu.edu/ee/smuphotonics/Gain/CoursePresentationFall03/Effective_Mass_Theory_July25-03.pdf** (accessed Aug. 2024).
62 H. Zhang, L. Liu and Z. Zhou, *RSC Adv.*, 2012, **2**, 9224–9229.
63 K. Ephraim Babu, N. Murali, K. Vijaya Babu, P. T. Shibeshi and V. Veeraiah, *Acta Phys. Pol., A*, 2014, **125**, 1179–1185.
64 Dielectric Constant What Does it Mean? **https://www.fauske.com/blog/dielectric-constant-what-does-it-mean** (accessed Jul. 2024).
65 Absorption Coefficient | PVEducation, **https://www.pveducation.org/pvcdrom/pn-junctions/absorption-coefficient** (accessed Jun. 2024).
66 C. Wang, S. Chen, J. Yang, L. Lang, H. Xiang, X. Gong, A. Walsh and S. Wei, *Chem. Mater.*, 2014, **26**, 3411–3417.
67 J. Buckeridge, D. Scanlon, A. Walsh and C. Catlow, *Comput. Phys. Commun.*, 2014, **185**, 330–338.
68 C. Freysoldt, B. Grabowski, T. Hickel, J. Neugebauer, G. Kresse, A. Janotti and C. Van De Walle, *Rev. Mod. Phys.*, 2014, **86**, 253–305.
69 L. Q. Chen, *MRS Bull.*, 2019, **44**, 520–523.
70 C. Persson, Y. J. Zhao, S. Lany and A. Zunger, *Phys. Rev. B: Condens. Matter Mater. Phys.*, 2005, **72**, 1–14.

71 Z. Huang, Z. Zheng, Z. Dai, X. Guo, S. Wang, L. Jiang, J. Wei and S. Chen, *J. Semicond.*, 2022, **43**, 042101.
72 Y. Kumagai, N. Tsunoda, A. Takahashi and F. Oba, *Phys. Rev. Mater.*, 2021, **5**, 123803.
73 R. Bystricky, T. K. Sameer, P. Hutár, V. L'ubomír and S. Milan, *Inorg. Chem.*, 2022, **61**, 18823–18827.
74 X. Du, Y. Liu, W. Pan, J. Pang, J. Zhu, S. Zhao, C. Chen, Y. Yu, Z. Xiao, G. Niu and J. Tang, *Adv. Mater.*, 2022, **34**, 2110252.
75 Y. Liang, Y. Zhang, J. Xu, J. Ma, H. Jiang, X. Li, B. Zhang, X. Chen, Y. Tian, Y. Han and Z. Shi, *Nano Res.*, 2023, **16**, 7867–7873.
76 J. Chang, H. Yuan, B. Wang, Y. Huang, X. Chen and H. Chen, *ChemPhysChem*, 2019, **20**, 489–498.
77 C. G. Van De Walle and J. Neugebauer, *J. Appl. Phys.*, 2004, **95**, 3851–3879.
78 NCI Australia (2019), Gadi Supercomputer, NCI Australia. (Service), DOI: **10.25914/608bfd1838db2**.

